Investigations of the Nature and Impact of Iron Contamination in Multicrystalline Silicon Solar Cell Materials

T. Buonassisi[1], .A.A. Istratov[1], M.Heuer[1,2], M.A. Marcus[3], B. Lai[4], Z.Cai[4], S.Heald[4], E.R.Weber[1]

[1]Univesity of California, Berkeley, CA, U.S.A; [2]University of Leipzig, Leipzig, Germany; [3]Lawrence Berkeley National Laboratory, Berkeley, CA, U.S.A.; [4]Argonne National Laboratory, Argonne, IL U.S.A.;

Introduction

Over 50% of the worldwide solar cell market is based on multicrystalline silicon (mc-Si). Even minute concentrations ($\sim 2 \times 10^{12}$ cm^{-3} of interstitial Fe (Fe$_i$) or $\sim 2 \times 10^{13}$ of iron-boron (Fe$_i$-B$_s$) pairs) of iron can reduce the minority carrier diffusion length in p-type silicon to 50 μm, unacceptable for most PV devices of reasonable efficiencies. Despite this fact, recent neutron activation analysis (NAA) data on commercially-available multicrystalline silicon (mc-Si) solar cell material revealed Fe concentrations of 10^{14} to 10^{16} cm^{-3} [1]. The question naturally arises as to how mc-Si can contain so much iron yet manage to achieve reasonable operating efficiencies. In this study, synchrotron-based microprobe techniques were applied to draw universal conclusions about the nature of Fe contamination in mc-Si via the systematic characterization of iron-rich precipitates and inclusions in this material.

Methods and Materials

Two types of mc-Si solar cell materials were used, grown by directionally-solidified cast technology (involves slow controlled solidification of 100-250 kg of melt in a crucible, with slow cooling of the ingot) and by sheet technology (a fast process used for fabrication of thin sheets of silicon). APS Beamlines 2-ID-D and 20-ID-B were employed in these investigations; additionally, some samples were pre-characterized at the Advanced Light Source at Lawrence Berkeley National Laboratory. The underperforming regions of the cell were identified by a large-area X-ray Beam Induced Current technique (XBIC) maps [2]. After a region of interest in the sample was identified by XBIC, X-ray fluorescence microscopy (μ-XRF) scans were performed with a much smaller step size to search for metal-rich clusters embedded in the silicon matrix. For typical experimental conditions with a 200 nm diameter beam and an accumulation time of 1 second, we have detected iron silicide clusters of radius 23±5 nm, while the noise-limited detection limit for the same conditions was estimated to be 16±3 nm for Fe particles near the sample surface. After metal-rich clusters of interest were located via μ-XRF, their chemical state was assessed via X-ray absorption microspectroscopy (μ-XAS).

Results and discussion

XBIC maps revealed certain grain boundaries with exceptionally high recombination activity in both processed (Fig. 1a) and unprocessed (not shown)

material. Multiple iron-rich clusters were detected by μ-XRF at these locations (see Fig. 1b). These iron-rich clusters populating grain boundaries can be divided into two distinct types. While the vast majority of iron-rich clusters were small (e.g. P1, P3, and P4 in Fig. 1, some rare clusters had nearly two orders of magnitude higher μ-XRF Fe counts (e.g. P2 in Fig. 1; note the log scale of Fe concentration).
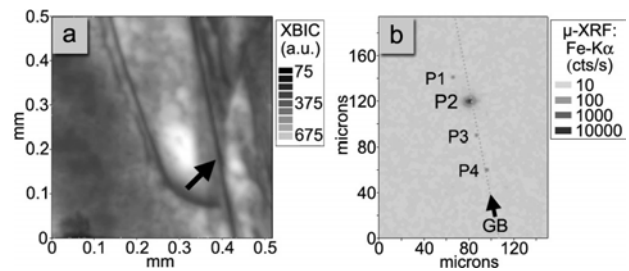
Fig. 1: *(a) Typical XBIC image of a cast mc-Si sample. The arrow in (a) points to a recombination-active grain boundary, a region of which was analyzed by μ-XRF in (b). Fe-rich clusters are found along the grain boundary, highlighted by the arrow and the dotted line in (b).*

An analysis by μ-XAS revealed that the clusters with smaller Fe counts were composed of iron-silicide (FeSi$_2$), while the clusters with much larger Fe counts were composed of oxidized iron (Fe$_2$O$_3$), as shown in Fig. 2.
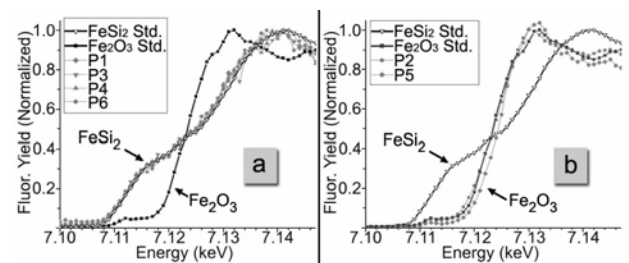
Fig. 2: *μ-XAS data discern two types of Fe-rich cluster in cast mc-Si material: (a) smaller iron silicide (FeSi$_2$) and (b) larger iron oxide (Fe$_2$O$_3$). Data labels correspond to precipitates in the μ-XRF image Fig. 1b.*

The compositions of these clusters were also different, as determined by the μ-XRF point scans. While the Fe$_2$O$_3$ clusters showed appreciable amounts of other contaminants such as Cr, Mn, and Ca (Fig. 3b), the smaller FeSi$_2$ clusters showed none of these above the μ-

XRF detection limit (Fig 3a). Only in as-grown material could Ni and Cu be found precipitated in the immediate vicinity of $FeSi_2$ in detectable quantities, but not Cr, Mn, Ti, or Ca.
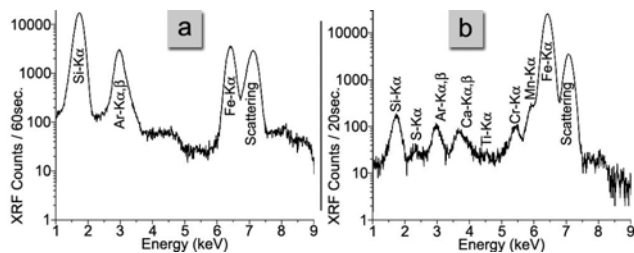
Fig. 3: *Typical μ-XRF point scans for the two types of Fe-rich clusters in cast mc-Si: (a) Smaller $FeSi_2$ clusters, without detectable quantities of other metals, and (b) larger Fe_2O_3 particles, wherein iron is accompanied by other elements reminiscent of ceramics, dirt, and stainless steel.*

The distributions of these clusters also differ. While the large Fe_2O_3 clusters are inhomogeneously distributed and are found in low density, the smaller $FeSi_2$ clusters appear to be fairly regularly spaced along the grain boundaries. We calculated a $FeSi_2$ precipitate density of $(1.5-2)\times10^6$ per cm^2 of grain boundary surface area.
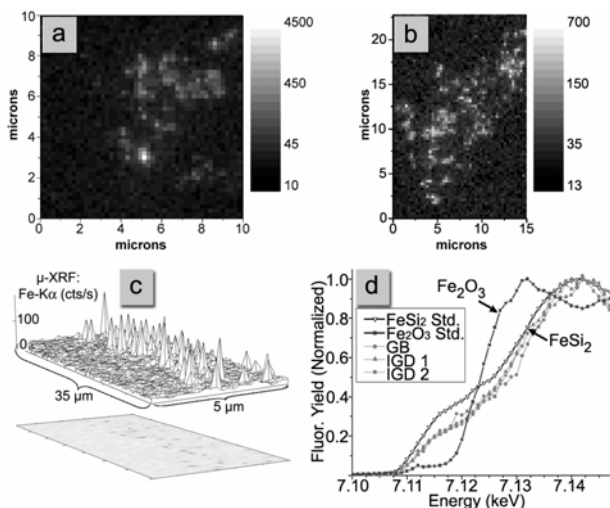

Figure 4: *(a, b) μ-XRF maps of the Fe distribution within typical intragranular defects in sheet material. (c) μ-XRF map of Fe nanoparticles within a typical grain boundary, shown in 3D (above) and in 2D projection (below). (d) The chemical state of the Fe particles shown in (a-c) is revealed by μ-XAS to be most similar to $FeSi_2$.*

Similar analysis of sheet material revealed (a) strongly recombination-active grain boundaries, and (b) localized intragranular defects. μ-XRF point spectra revealed Fe present en masse at both these locations, with a small contribution from Cr in the case of certain intragranular

defects. High-resolution μ-XRF maps revealed that the intragranular defects were irregular in shape and consisted of an agglomeration of many nanoparticles, as shown in Figs. 4a and 4b. The grain boundaries were also decorated by Fe-rich nanoparticles, as shown in Fig. 4c. The chemical states of these particles were measured by μ-XAS; by comparison with standard material, it is deduced that Fe is most likely to be in the form of iron silicide, as shown in Fig. 4d. The spacing and average size of the iron silicide precipitates along the grain boundaries of this material were significantly homogeneous. The particle density along the surface of the grain boundary was determined to be within the range of $(1-2)\times10^7$ cm^{-2}.

Several systematic material-independent trends were observed, as described above, which allowed us to make conclusions about the origins of metal contamination in mc-Si, the physical mechanisms involved in incorporating large amounts of Fe into mc-Si, and the formation of the iron-rich clusters observed by μ-XRF. Fig. 5 presents a pictorial summary of these processes.
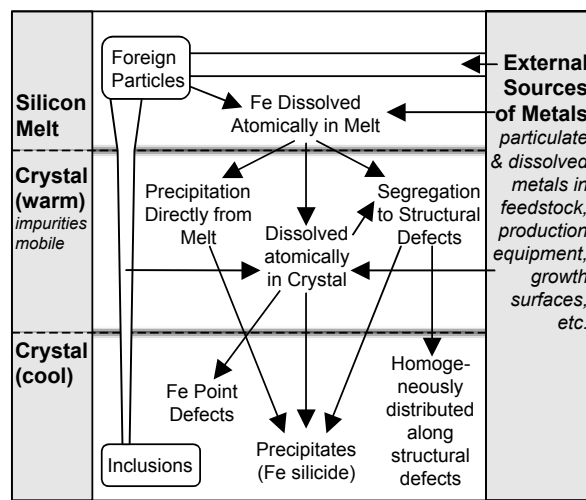

Fig. 5: *Graphical representation of the origins of Fe contamination in mc-Si and the physical mechanisms responsible for incorporating large amounts of iron.*

We deduced (a detailed discussion will be published elsewhere) the origins of metals in most mc-Si materials likely include some combination of the following: metals dissolved in the silicon feedstock, foreign metallic particles introduced with the feedstock, metals originating from furnace or production equipment, and metals diffusing from the walls of the crucible or growth surfaces. As shown in Fig. 5, there are (at least) five pathways for incorporating Fe into the warm mc-Si material: (a) direct incorporation of incompletely dissolved foreign metal-rich particles into the crystal as inclusions, (b) direct precipitation of locally supersaturated iron from the melt, (c) segregation of metals dissolved in the melt to structural defects, (d) incorporation of dissolved Fe in the melt into single-crystalline regions of the material as interstitial atoms,

and (e) diffusion of Fe from the growth surfaces into the crystal. Large amounts of iron can be incorporated into mc-Si via three primary mechanisms: (a) the direct incorporation of incompletely dissolved large, foreign metal-rich particles into the crystal as inclusions, (b) the possibility of direct precipitation of locally supersaturated iron from the melt at regions of the solid-liquid interface sheltered from the convective flow of the melt, and (c) the segregation of metals to structural defects.

Besides incorporation of iron during ingot/sheet growth, we studied the processes of dissolution of metal clusters during rapid thermal processing (RTP), often used for emitter diffusion during fabrication of solar cells.
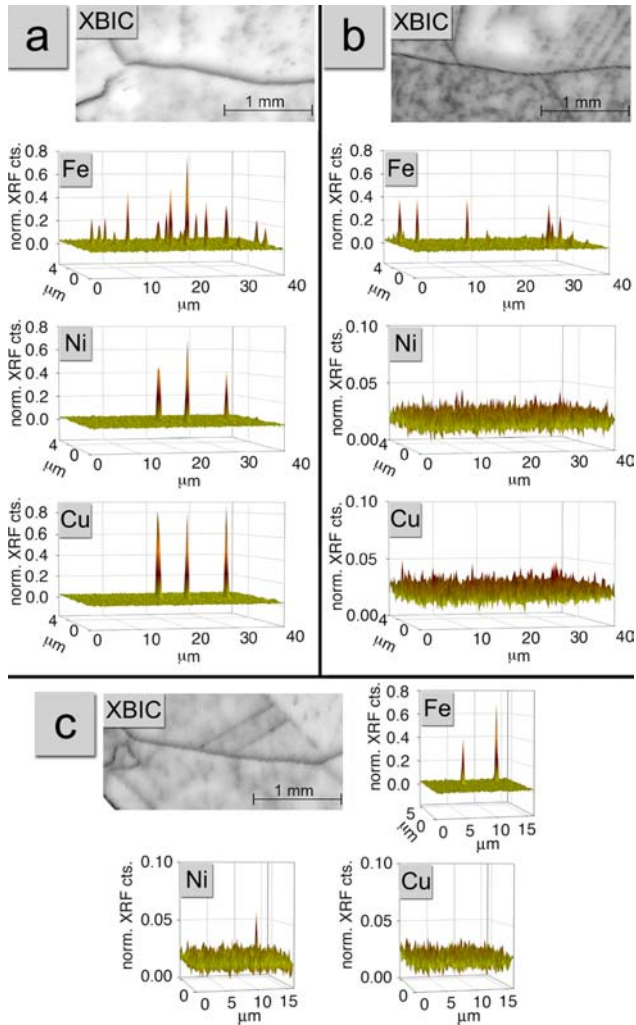
Fig. 6: Analysis of the metal content and distribution at grain boundaries in three sister wafers: (a) Unprocessed material (as-grown), (b) High-T RTP (1000°C, 20s), and (c) Low-T RTP (860°C, 120s).

Three sister wafers of cast mc-Si, i.e. adjacent vertical slices of the ingot, with virtually identical initial crystal structure, were selected for this analysis. The first wafer was left unprocessed and was used as a reference. The second and the third wafers were processed into solar cells using different temperatures for emitter diffusion from a phosphorus spin-on source. The second wafer was processed at 860°C for 120 seconds, while the third wafer was processed at a higher temperature, 1000°C for 20 seconds. Different annealing times were chosen to obtain comparable emitter depths. The solar cells fabricated using low-temperature (860°C) RTP was found to be 20% (rel.) more efficient than the cell fabricated using high-temperature (1000°C) RTP.

A characteristic region of material was extracted for synchrotron-based analytical studies from the same location in all three sister wafers. In as-grown material, six iron precipitates were analyzed, which had 543, 432, 531, 520, 486, and 323 counts. In low-temperature RTP sample (860°C, 120 s) the analyzed iron precipitates had 380 and 579 counts. Finally, in high-temperature RTP (1000°C, 20s) sample the analyzed iron precipitates had 220, 287, 335, 134, 256, and 209 counts. Comparison of these samples led us to the following observations: (1) In the *as-grown material*, multiple iron-silicide clusters can be seen decorating the grain boundary. Some copper and nickel precipitates were also observed, although in lower spatial densities. (2) In the "low-temperature RTP" sample, some large $FeSi_2$ precipitates remain, with the same count rate as in the as-grown material. Cu_3Si precipitates are no longer detectable. Ni-precipitates decreased in size. (3) In the "high-temperature RTP" sample, $FeSi_2$ precipitates were detected, but their intensities are much reduced. Precipitates in the high-T RTP sample consistently demonstrate Fe contents 50% less than as-grown material, giving evidence for iron silicide precipitate dissolution. No Cu- nor Ni-rich precipitates were observed.

From these observations, we concluded that when the rapid cooling occurs at the end of the RTP anneal, metals dissolved from the precipitates become "trapped in", forming smaller and more distributed recombination centers (precipitates and point defects). This leads to a decrease in solar cell performance. To overcome this performance degradation, one should either use lower-temperature anneals to leave iron-silicide precipitates undisturbed, or use longer high-temperature treatments to completely dissolve iron-silicide precipitates and getter the dissolved iron. However, long high-temperature anneals may be incompatible with diffusion of shallow emitter layers.

1. A. A. Istratov, T. Buonassisi, R. J. McDonald, A. R. Smith, R. Schindler, J. A. Rand, J. P. Kalejs, and E. R. Weber, *J. Appl. Phys.* **94**, 6552 (2003).
2. O. F. Vyvenko, T. Buonassisi, A. A. Istratov, H. Hieslmair, A. C. Thompson, R. Schindler, and E. R. Weber, *J.Appl.Phys.* **91**, 3614 (2002).